



Cite as

Nano-Micro Lett.
(2025) 17:133Received: 20 October 2024
Accepted: 2 January 2025
© The Author(s) 2025

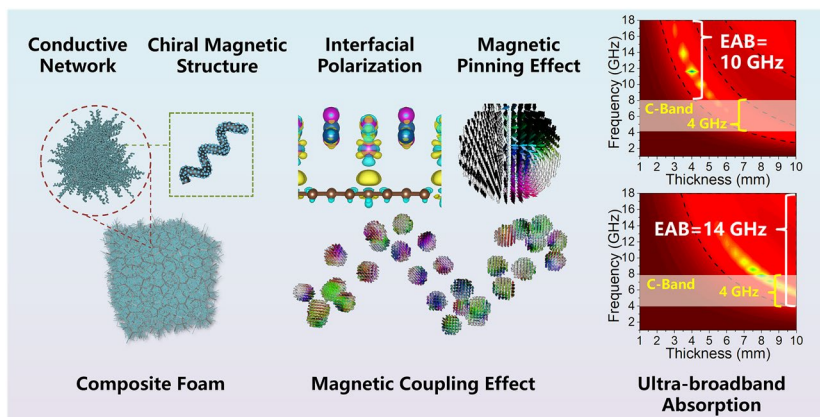
Multifunctional Carbon Foam with Nanoscale Chiral Magnetic Heterostructures for Broadband Microwave Absorption in Low Frequency

Hao Zhang¹, Kaili Kuang¹, Yifeng Zhang¹, Chen Sun¹, Tingkang Yuan¹, Ruilin Yin¹, Zeng Fan¹, Renchao Che² ✉, Lujun Pan¹ ✉

HIGHLIGHTS

- A novel multifunctional carbon foam with nanoscale chiral magnetic heterostructures is constructed, in which the interconnection network provides strong conduction loss.
- The interfacial polarization loss induced by the FeNi-carbon interfaces is confirmed by the density functional theory calculations, and the magnetic pinning and coupling effects are revealed by the micromagnetic simulation.
- The composite foam exhibits an ultrabroad effective absorption bandwidth (EAB) of 14 GHz and a C-band EAB of 4 GHz, achieving the full C-band coverage.

ABSTRACT The construction of carbon nanocoil (CNC)-based chiral-dielectric-magnetic trinity composites is considered as a promising approach to achieve excellent low-frequency microwave absorption. However, it is still challenging to further enhance the low frequency microwave absorption and elucidate the related loss mechanisms. Herein, the chiral CNCs are first synthesized on a three-dimensional (3D) carbon foam and then combined with the FeNi/NiFe₂O₄ nanoparticles to form a novel chiral-dielectric-magnetic trinity foam. The 3D porous CNC-carbon foam network provides



excellent impedance matching and strong conduction loss. The formation of the FeNi-carbon interfaces induces interfacial polarization loss, which is confirmed by the density functional theory calculations. Further permeability analysis and the micromagnetic simulation indicate that the nanoscale chiral magnetic heterostructures achieve magnetic pinning and coupling effects, which enhance the magnetic anisotropy and magnetic loss capability. Owing to the synergistic effect between dielectricity, chirality, and magnetism, the trinity composite foam exhibits excellent microwave absorption performance with an ultrabroad effective absorption bandwidth (EAB) of 14 GHz and a minimum reflection of loss less than -50 dB. More importantly, the C-band EAB of the foam is extended to 4 GHz, achieving the full C-band coverage. This study provides further guidelines for the microstructure design of the chiral-dielectric-magnetic trinity composites to achieve broadband microwave absorption.

KEYWORDS Carbon nanocoils; Chiral magnetic structures; 3D conductive networks; Magnetic pinning effect; Broadband microwave absorption

✉ Renchao Che, rcche@fudan.edu.cn; Lujun Pan, lpan@dlut.edu.cn¹ School of Physics, Dalian University of Technology, Dalian 116024, Liaoning, People's Republic of China² Laboratory of Advanced Materials, Shanghai Key Lab of Molecular Catalysis and Innovative Materials, Department of Materials Science, Fudan University, Shanghai 200438, People's Republic of China

Published online: 06 February 2025



SHANGHAI JIAO TONG UNIVERSITY PRESS

Springer

1 Introduction

Electronic devices and systems based on the fifth-generation (5G) technologies bring great convenience to daily life. However, the electromagnetic wave interference/radiation is also becoming a potential threat [1–3]. Multitudinous microwave absorption materials with excellent absorption performance have been developed, most of which exhibit wide effective absorption bandwidth (EAB) in the high microwave frequency region (10–18 GHz) [4–7]. Nevertheless, the 5G technologies signals fall in the low microwave frequency region (2–10 GHz), especially in the C-band (4–8 GHz). Therefore, further expanding the low frequency absorption bandwidth of the microwave absorption materials is critical but remains challenging.

It is anticipated that magnetic materials with superior natural resonance [8] and exchange resonance [9] would be effective in achieving excellent low-frequency microwave absorption, owing to their strong magnetic loss ability. However, it is difficult to further improve the magnetic loss ability of the magnetic materials due to the Snoke's limit [10]. Geometric regulation, particularly the construction of magnetic anisotropic assemblies, is an efficient strategy for promoting the Snoke's limit. For example, Che et al. designed the nonsymmetric hammer-shaped Fe/Fe₃O₄@SiO₂ composite, achieving strong magnetic loss ability [11]. The nonsymmetric distribution of the magnetic components is beneficial to enhance the magnetic anisotropy, which further promotes the Snoke's limit. Moreover, the magnetic anisotropy is also affected by the compositional discrepancy of the magnetic components. Magnetic heterostructures, especially at the nanoscale, have great potential for enhancing the magnetic anisotropy. Wang et al. constructed the ferromagnetic/antiferromagnetic heterostructures, confirming that magnetic pinning effect induced by the interfacial magnetic bias improves the magnetic anisotropy and low frequency permeability [12]. Therefore, achieving the nonsymmetric distribution of the nanoscale magnetic heterostructures could be an effective strategy to promote the Snoke's limit. Furthermore, the high density of the magnetic materials results in a high filling ratio in the absorbers, which is disadvantageous for their applications. It is also important to combine magnetic materials with a lightweight dielectric material that can simultaneously achieve strong magnetic loss and low density.

Carbon nanocoils (CNCs) have been considered as a kind of versatile nanomaterial in many fields [13–27]. Compared to other carbon materials such as graphene, carbon nanotubes and carbon nanofibers, the CNCs have moderate conductivity, which is beneficial for adjusting impedance matching. The point-to-point contact between CNCs also prevents them from aggregation to form a uniformly dispersed composite. More importantly, the CNCs possess obvious 3D helical morphology, which provides the excellent chiral template for magnetic components. The nanoscale line diameter and the helical structure of the CNCs could contribute to the confined space synthesis of the magnetic heterostructures. Besides, the unique chiral morphology of the CNCs could also give rise to the nonsymmetric distribution of the magnetic heterostructures. Therefore, the CNCs are considered as the excellent template materials for construction of the chiral magnetic absorbers. Although various magnetic/CNC composites, including Fe₃O₄/Al₂O₃/CNC [28], FeCo@FeCo₂O₄/CNC [29], and CoNi/CNC [30], have been developed and achieved excellent microwave absorption performance, the EAB in the low frequency range still requires further extension. The internal mechanisms of enhanced magnetic loss also remain to be investigated. In addition, most of the current magnetic/CNC composites are in the form of powder, which require additional support matrix and exhibit narrow band impedance matching. It is believed that the three-dimensional (3D) porous structures such as foams and aerogels tend to broaden the impedance matching range [31–33]. In the porous structures, the presence of air reduces the permittivity, which contributes to the excellent impedance matching. Meanwhile, the efficient interconnected networks ensure the conduction loss and avoid the agglomeration. Therefore, if the chiral magnetic units are uniformly arranged in a 3D porous interconnected network, the microwave absorption performance would be improved significantly.

In this work, the chiral CNCs are first synthesized on a three-dimensional (3D) carbon foam and then combined with the FeNi/NiFe₂O₄ nanoparticles to form a novel chiral-dielectric-magnetic trinity foam via chemical vapor deposition (CVD) and solvothermal reactions. The porous CNC-carbon foam skeleton forms an 3D interconnected conductive network. The nanoscale FeNi/NiFe₂O₄ magnetic heterostructures, in which the FeNi acts as the ferromagnetic component while the NiFe₂O₄ acts as the ferrimagnetic component, are uniformly synthesized on the chiral CNC.

The FeNi/carbon interfaces contribute to the interfacial polarization loss. Meanwhile, the formation and nonsymmetric distribution of the nanoscale magnetic heterostructures lead to the magnetic pinning and coupling effect, which promotes the Snoke's limit and increases the magnetic loss. With the synergistic effect between chirality, magnetism and dielectricity, the composite carbon foam exhibits superior microwave absorption performance in both low and high frequencies.

2 Experimental Section

2.1 Materials

Deionized water, ethanol, and nickel nitrate ($\text{Ni}(\text{NO}_3)_2 \cdot 6\text{H}_2\text{O}$) were purchased from Tianjin Kermel Chemical Reagent Co., Ltd. Ferrous sulfate ($\text{FeSO}_4 \cdot 7\text{H}_2\text{O}$) and hexamethylenetetramine (HMT) were purchased from Shanghai Sinopharm Chemical Reagent Co., Ltd. Melamine foam was provided by Shanghai Junhua Hightech Materials Co., Ltd. All chemical reagents were of analytical grade and were used without further purification.

2.2 Preparation of CF, CCF, FCF, and FCCF Composites

2.2.1 Preparation of Carbon Foam (CF)

The carbon foam samples were obtained through the carbonization of the melamine foams. Typically, the melamine foams were placed in a tube furnace (BTF-1200C-III-S, Anhui BEQ) under an Ar atmosphere of 492.5 sccm. The foam samples were heated to 700 °C at a heating rate of 5 °C min^{-1} and then carbonized at 700 °C for two hours. Finally, the carbon foams were collected and labeled as CF.

2.2.2 Preparation of Carbon Nanocoil/Carbon Foam (CCF) Composites

As shown in Fig. 1, the CNC/CF composites were prepared by the CVD process. Briefly, the Fe-Sn-O catalyst was prepared according to our previous research [34, 35] and dispersed in ethanol. The as-prepared CF samples were immersed in the Fe-Sn-O catalyst dispersion and dried at

60 °C for 2 h. Then, the CF samples coated with catalyst were placed in the tube furnace under 563.2 sccm Ar atmosphere. Finally, the CNCs were synthesized on the CF samples with the introduction of additional 23.24 sccm C_2H_2 gases at 710 °C and the CNC/CF (denoted as CCF) composites were obtained.

2.2.3 Preparation of FeNi@NiFe₂O₄@CNC/CF (FCCF) and FeNi@NiFe₂O₄/CF (FCF) Composites

Generally, 2 mmol $\text{Ni}(\text{NO}_3)_2 \cdot 6\text{H}_2\text{O}$, 1 mmol $\text{FeSO}_4 \cdot 7\text{H}_2\text{O}$, and 4 mmol HMT were added into 40 mL mixed solvent of ethanol and deionized water (volume ratio was 1:1). The mixture was then stirred for 20 min to form the precursor solution. The as-prepared CCF composites were functionalized by the plasma treatment for 10 min. The functionalized CCF composites and the precursor solution were transferred into a 50-mL Teflon-lined autoclave and then subjected to a solvothermal reaction at 100 °C for 10 h. After the reaction, the FeNi@NiFe₂O₄@CNC/CF precursors were washed with deionized water and dried at 60 °C overnight. According to our previous research [29], an annealing temperature of 700 °C is chosen to ensure the formation of the FeNi/NiFe₂O₄ magnetic heterostructures. Finally, the FeNi@NiFe₂O₄@CNC/CF precursors were annealed at 700 °C for 2 h under 492.5 sccm Ar atmosphere to prepare the FeNi@NiFe₂O₄@CNC/CF composites, labeled as FCCF-1. Repeatedly, the precursor solutions were used at 1.5 times and twice the concentration to prepare two other FeNi@NiFe₂O₄@CNC/CF composites, denoted as FCCF-2 and FCCF-3, respectively. All other conditions remained unchanged. For comparison, the FeNi@NiFe₂O₄/CF composites (denoted as FCF) were also prepared by changing the CCF composites as pure CF samples. All other conditions were kept unchanged.

2.3 Characterization

Morphological and microstructural information of the samples was obtained using a field emission scanning electron microscopy (SEM, SEM5000, CIQTEK Co., Ltd.) and a transmission electron microscopy (TEM, JEM F-200, JEOL). X-ray diffraction (XRD, Lab XRD-7000 s) with a Cu K α radiation source was used to characterize the

crystal structure of the composites. Raman spectroscopy (Finder930, Zolix) was used to study the chemical states of the composites. The magnetic properties of the samples were obtained using a vibrating sample magnetometer (VSM, LakeShore 7400S). The electromagnetic parameters were measured using a vector network analysis (VNA, Keysight E5080B) in the frequency range of 1–18 GHz. The composites were cut into a coaxial ring shape with an external diameter of 7.00 mm, an internal diameter of 3.04 mm and a thickness of 2.0 mm. The prepared coaxial ring samples were then used directly for the measurement of the electromagnetic parameters without any supporting matrix.

3 Results and Discussion

3.1 Morphology and Structure Information of the Samples

The microstructures and morphologies of the as-prepared samples are depicted in the SEM images (Figs. 2 and S1). The initial CF sample exhibits a typical 3D interconnecting network formed by the carbon fibers with the diameter of about 5 μm (Figs. 2a and S1a). It is considered that the 3D interconnective skeleton has been successfully established by the carbon foam. As shown in Fig. 2b, c, lots of CNCs grow uniformly on the carbon foam skeleton after the CVD process. The CF-CNC structures form a denser

interconnection network, which further enhances the electron transfer capability of the composite. In addition, the formation of the CF-CNC structures also improves the specific surface area of the composite, which gives rise to the multiple scattering of the microwave. In Fig. 2d, it is observed that the CNCs exhibit an obvious chiral helical morphology, which provide the excellent chiral templates for the fabrication of the chiral magnetic structures. Moreover, the helical diameter of the synthesized CNCs varies from 100 to 500 nm, which is beneficial for the construction of the multi-scale composite. It is believed that the multi-scale composites tend to achieve multi-band absorption effect, which is beneficial for further expanding the EAB of the absorbers. Figure 2e shows that the 3D interconnection network could be well maintained during the solvothermal reaction and the annealing treatment. Furthermore, the FeNi-based magnetic nanoparticles are synthesized uniformly on the surface of the CNCs, forming the chiral magnetic structures (Fig. 2f–h). Furthermore, it is also observed in Fig. 2f–h that the growth density and size of the FeNi-based nanoparticles increase gradually as the concentration of the precursor solution rises. However, without the CNCs, the FeNi-based particles would grow on the carbon fiber skeleton directly with a diameter of around 200–500 nm, which tend to aggregate with each other (Fig. S1b–d). Therefore, it is reasonable to conclude that the curved surface and the small line diameter endow the CNCs with the confinement effect, which not only contributes to the formation of the

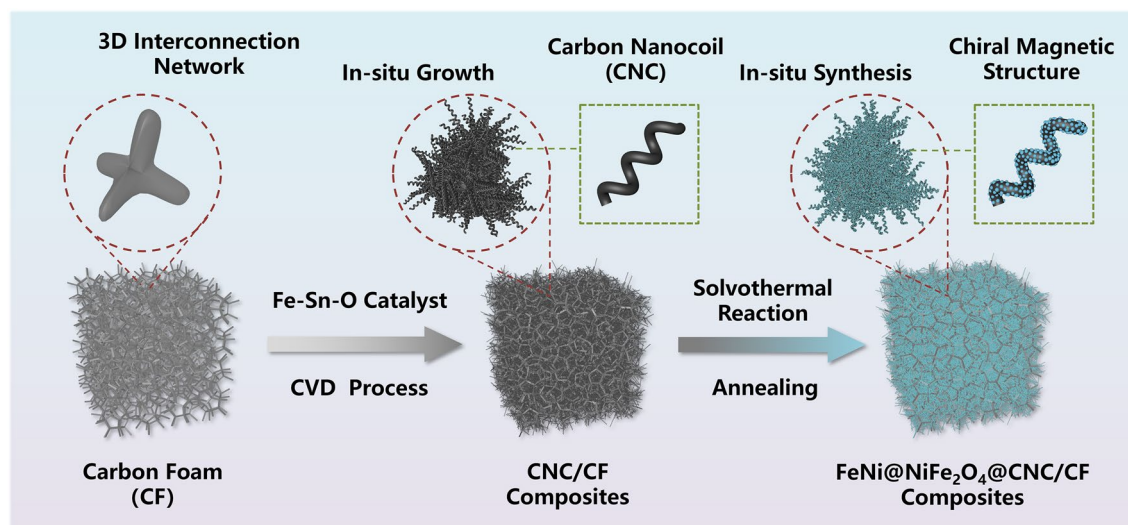


Fig. 1 Schematic illustration of synthesis process for the CCF and FCCF samples

nanoscale FeNi-based particles, but also prevents the nanoparticles from aggregation.

The morphology and structural information of the FeNi@CNC units in the FCCF-2 sample are further shown in the TEM images (Fig. 3a–d). The FeNi@CNC unit shows an obvious chiral structure with the uniform distribution of the FeNi-based nanoparticles (Fig. 3a, b), which is consistent with the SEM results. Besides, the HR-TEM image of the internal part of the nanoparticle (Fig. 3c) exhibits the lattice fringes with an interplanar spacing of 0.29 nm, corresponding to the (220) crystal plane of NiFe_2O_4 . The relatively blurred lattice fringes reveal the weak crystallinity of the NiFe_2O_4 . It could therefore be surmised that additional reactions may occur during the annealing treatment, resulting in the destruction of the lattice structure of the NiFe_2O_4 . Furthermore, the HR-TEM image of the nanoparticle surface (Fig. 3d) shows a lattice fringe with an interplanar spacing of 0.20 nm, corresponding to the (111) crystal plane of FeNi. Moreover, another crystalline structure is also observed in Fig. 3d. The interplanar spacing is measured as 0.34 nm, corresponding to the (002) crystal plane of graphite carbon. Therefore, during the annealing treatment, the NiFe_2O_4 is partially reduced to the metal FeNi by the carbon due to the carburization effect [36], resulting in the formation of the FeNi/ NiFe_2O_4 magnetic heterostructure and the metal–carbon heterointerface. The Raman spectra of the samples were tested to confirm this conclusion. As shown in Fig. 3e, the CF and CCF samples do not exhibit any peak in the 0–1000 cm^{-1} region. For the FCCF and FCF composites,

the introduction of the FeNi-based particles results in the appearance of three main peaks appearing at 480, 570, and 683 cm^{-1} , which correspond to the $T_{2g}(1)$, $T_{2g}(2)$, and A_{1g} vibrational modes of the NiFe_2O_4 [37, 38]. The Raman results further confirm the existence of the NiFe_2O_4 in the FeNi-based particles, which is consistent with the TEM images. Moreover, the XRD patterns of the FCCF and FCF samples (Fig. 3f) provide further structural information of the FeNi-based particles. It is observed that the FCCF and FCF samples exhibit three obvious diffraction peaks at 44.1°, 51.4°, and 75.7°, corresponding to the (111), (020), and (022) crystal planes of the metal FeNi (JCPDS No. 96-152-4834). The sharp diffraction peaks indicate that the metal FeNi possesses good crystallinity, which is consistent with Fig. 3d. It is also worth noting that the XRD patterns do not exhibit any characteristic peak of the NiFe_2O_4 , confirming that the NiFe_2O_4 in the FeNi-based particles possesses weak crystallinity (Fig. 3c). In addition, a prominent peak at 25.6° appears in the XRD pattern of the FCCF-2 sample, corresponding to the (002) crystal plane of graphitic carbon. It is confirmed that the synthesis of the CNCs improves the electron transfer capability of the carbon-based network. As illustrated in Fig. S2a, b, the XRD and Raman spectra of the FCCF-1 and FCCF-3 samples exhibit a high degree of consistency with the XRD and Raman spectra of the FCCF-2 sample, indicating that the FeNi/ NiFe_2O_4 magnetic heterostructures are also synthesized in the FCCF-1 and FCCF-3 samples. In a word, the 3D interconnection network with the chiral magnetic units has been successfully established,

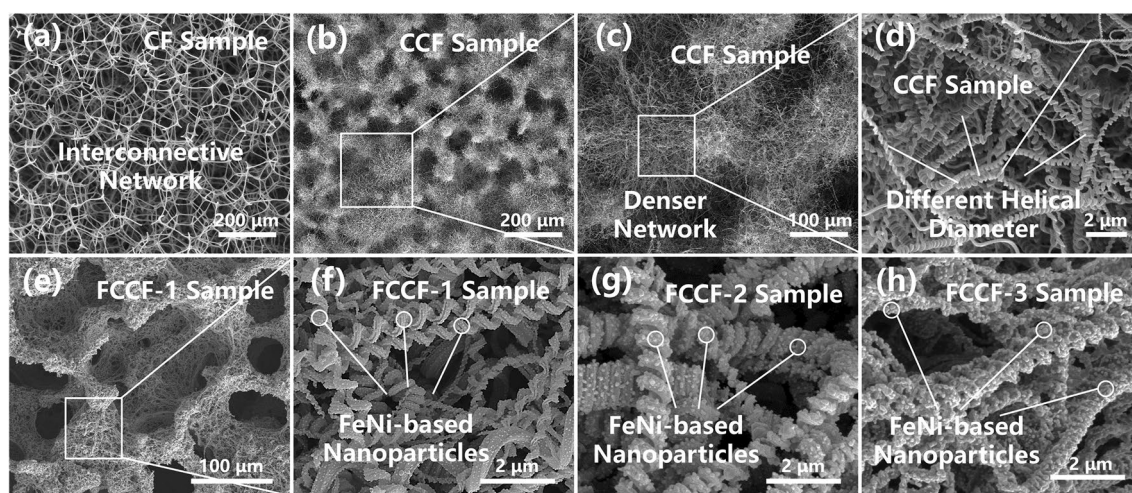


Fig. 2 SEM images of **a** CF sample, **b–d** CCF sample, **e, f** FCCF-1 sample, **g** FCCF-2 sample, and **h** FCCF-3 sample

exhibiting excellent electron transfer capability and a multitude of FeNi/NiFe₂O₄ magnetic heterostructures.

Impedance matching (Z) is considered the primary factor for excellent microwave absorbers, since the Z represents the ability of microwaves to enter the interior of the absorber [39–42]. The Z value is calculated according to the following formula [43–47]:

$$Z = \frac{Z_{in}}{Z_0} = \sqrt{\left| \frac{\mu_r}{\epsilon_r} \right|} \tanh \left[j(2\pi fd/c) \sqrt{\mu_r \epsilon_r} \right] \quad (1)$$

where Z_{in} and Z_0 refer to the input impedance of the microwave absorber and the free space, respectively; f represents the frequency of microwave; d is the thickness of the

microwave absorber; and c stands for the velocity of light. It is observed in the formula that the Z value is closely related to the complex permittivity ($\epsilon_r = \epsilon' - j\epsilon''$) and permeability ($\mu_r = \mu' - j\mu''$), in which the real parts (ϵ' and μ') refer to the electric and magnetic energy storage capacities, while the imaginary parts (ϵ'' and μ'') represent the energy dissipation capacities [48, 49]. Thus, the electromagnetic parameters of the samples are tested (Fig. S3) and the Z values of the samples are further calculated (Figs. 3g–j and S4). Generally, a Z value of 1 means that all the microwaves could enter the interior of the absorber without reflection. Accordingly, a Z value between 0.8 and 1.2 (close to 1) is essential to produce superior microwave absorbers. In Fig. 3g, h, the impedance matching of the CF and CCF is poor due to their inadequate or excessive permittivity value. For the FCF sample, the

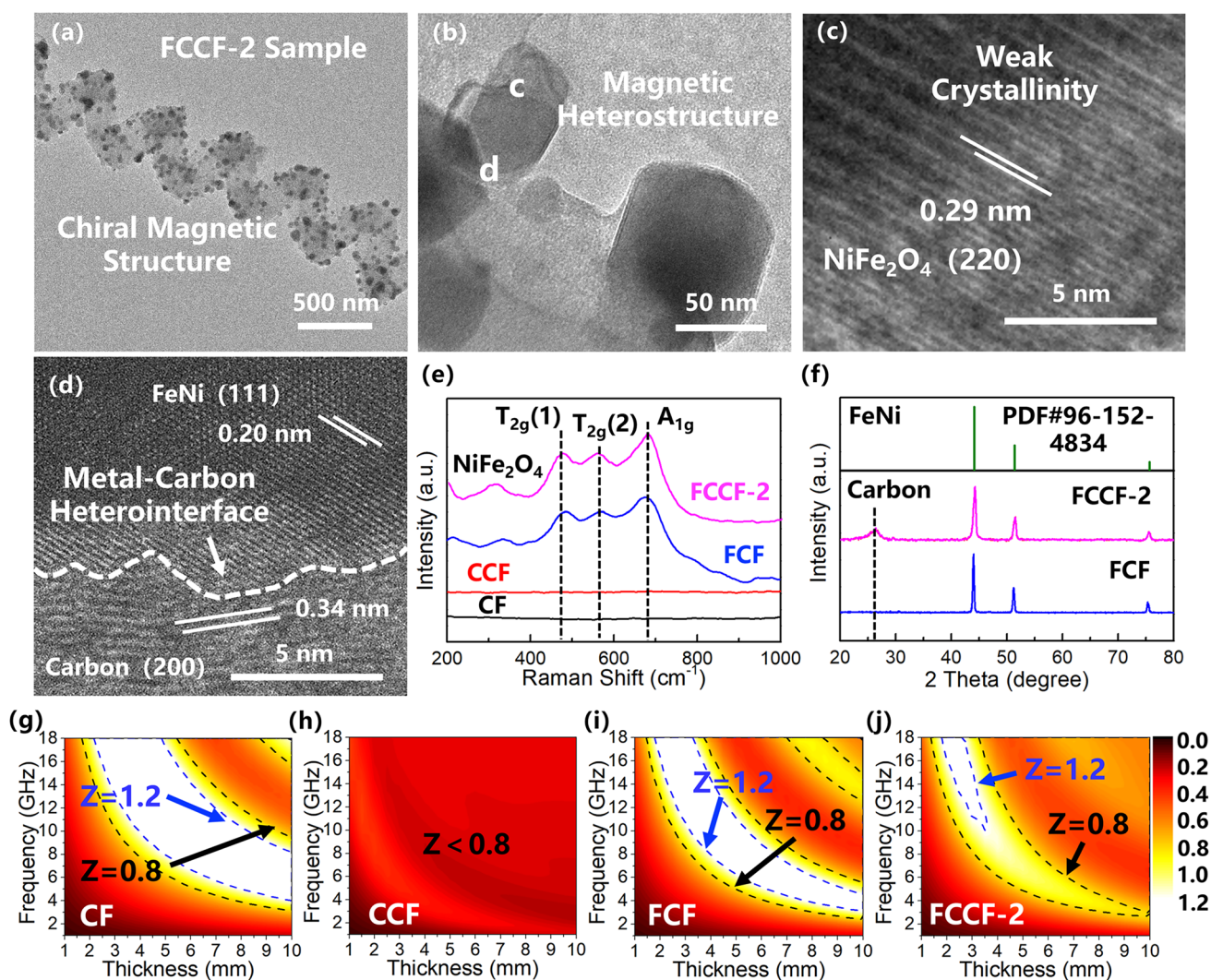


Fig. 3 a, b TEM and c, d HRTEM images of the FCCF-2 composites; e Raman spectra of the CF, CCF, FCF, and FCCF-2 composites; f XRD patterns of the FCF and FCCF-2 composites; Impedance matching contour maps of g CF, h CCF, i FCF, and j FCCF-2 samples

introduction of the FeNi/NiFe₂O₄ particles modulates the permittivity, which promotes the impedance matching in some degree (Fig. 3i). Furthermore, Figs. 3j and S4 illustrate that the impedance matching of the FCCF composites is greatly promoted by the introduction of the CNCs and FeNi/NiFe₂O₄ nanoparticles. Among the samples, the FCCF-2 exhibits the optimal impedance matching. Therefore, it is concluded that the CNCs and FeNi-based nanoparticles effectively collaborate with each other in permittivity modulation, contributing to good impedance matching.

3.2 Microwave Absorption Performance and Multifunctional Properties of the Samples

The RL value is the most used index for evaluating the microwave absorption performance of absorbers. According to the transmission line theory, the formula for calculating the RL value is as follows [50–52]:

$$RL(\text{dB}) = 20 \log \left| \frac{Z_{\text{in}} - Z_0}{Z_{\text{in}} + Z_0} \right| \quad (2)$$

As shown in Fig. S5, the CF (Fig. S5a, c) and CCF (Fig. S5b, d) samples exhibit low RL values and inadequate microwave absorption performance, which can be attributed to the suboptimal impedance matching. For the FCF sample (Fig. 4a, e), the microwave absorption performance gets better in some degree because of the promoted impedance matching. The minimum RL reaches -19 dB, and the maximum EAB is 5.4 GHz. It is also observed in Fig. 4g that the EAB value in C-band reaches 3.1 GHz, confirming that the 3D magnetic foam structure has potential in low frequency microwave absorption. Furthermore, the FCCF-1 sample (Fig. 4b, f) achieves a broad EAB of 9.2 GHz with a thickness of 3.5 mm, indicating that the chiral magnetic units are beneficial for extending the EAB. The C-band EAB of the FCCF-1 sample reaches 2.9 GHz. In addition, the FCCF-2 sample (Fig. 4c, g), with a higher density of magnetic nanoparticles, shows a wider EAB of 10 GHz with a thickness of 4 mm. More importantly, the C-band EAB of the FCCF-2 sample is also expanded to 4 GHz, achieving the full C-band coverage. With the further increase in the growth density of the magnetic nanoparticles, the FCCF-3 sample (Fig. 4d, h) achieves an ultrabroad EAB of 14 GHz. However, the corresponding thickness rises to 10 mm, which is much thicker than the FCCF-2 sample. In a word, the FCCF samples all

exhibit superior microwave absorption performance compared with the FCF sample. On the one hand, the excellent microwave absorption performance of the FCCF samples is attributed to their better impedance matching. On the other hand, the introduction of the CNCs and the magnetic heterostructures further enhances the dielectric and magnetic losses. As shown in Fig. 4i, it is concluded that the FCCF samples achieve both high EAB and C-band EAB values compared to the carbon-based 3D aerogel/foam absorbers in other studies [53–61]. Therefore, the FCCF samples could exhibit excellent microwave absorption performance in both low frequency and high frequency regions.

To further evaluate the actual far-field microwave absorption performance of the FCCF samples in real situations, radar cross section (RCS) simulations are performed based on the electromagnetic parameters. In general, theta and phi in spherical coordinates determine the scattering direction of the RCS value (σ) for a given scattering source as follows [62–65]:

$$\sigma(\text{dBm}^2) = 10 \log \left[\frac{4\pi S}{\lambda^2} \left| \frac{E_S}{E_i} \right|^2 \right] \quad (3)$$

where E_S and E_i refer to the electric field intensities of the accepting wave; λ represents the wavelength of the incident microwave; and S stands for the area of the simulated plate. The RCS is the parameter used to quantify the echo intensity of a target material when illuminated by radar waves. Consequently, a weaker RCS signal indicates a greater microwave absorption capability of the sample. In this study, RCS simulations are performed using the CST STUDIO SUITE 2019 software, with the positive x-axis set as the direction of the microwave. As shown in Fig. 5j, the pristine perfect electric conductor (PEC) plate exhibits strong RCS scattering signal, indicating weak microwave absorption capability. However, the PEC plate coated with the FCF sample shows lower scattering signal due to the microwave absorption capability of the FCF sample. Furthermore, the FCCF-2/PEC model exhibits the lowest scattering signal, revealing that the FCCF-2 sample possesses the strongest microwave absorption capability. Due to the consistency of the measured microwave absorption results and the RCS simulation results, it is reasonable to conclude that the FCCF-2 composites show great potential for practical applications as excellent microwave absorbers.

In addition to the microwave absorption performance, the FCCF-2 composites also possess multifunctional properties. As shown in Fig. S6a, the FCCF-2 sample could easily be perched on top of a dandelion without deforming the soft dandelion seeds, indicating the ultra-lightweight and low-density characteristics of the FCCF sample. Figure S6b shows that the FCCF-2 sample exhibits obvious magnetic properties, which is beneficial for improving the magnetic loss. Furthermore, the FCCF-2 sample could maintain its structure without mechanical damage even under a load of 3000 times its own weight (Fig. S6c), owing to its excellent structural robustness. As shown in Fig. 4k, when the 5-mm-thick FCCF-2 sample is placed on

the heating platform with the temperature set at 100, 120, and 150 °C, respectively, the surface temperatures of the FCCF-2 sample are only 65, 71, and 86 °C, respectively. Moreover, the surface temperature of FCCF-2 remains stable at around 60 °C as the heating time is increased (Fig. S7). Therefore, it is considered that the FCCF-2 sample possesses excellent thermal insulating performance. Furthermore, the Joule heating performance of the FCCF-2 sample is investigated by applying a voltage to both ends of the foam. The infrared thermal images shown in Fig. 4l intuitively indicate the surface temperature of the FCCF-2 sample under different voltages. At voltages of 5–25 V, the FCCF-2 sample exhibits excellent Joule heating

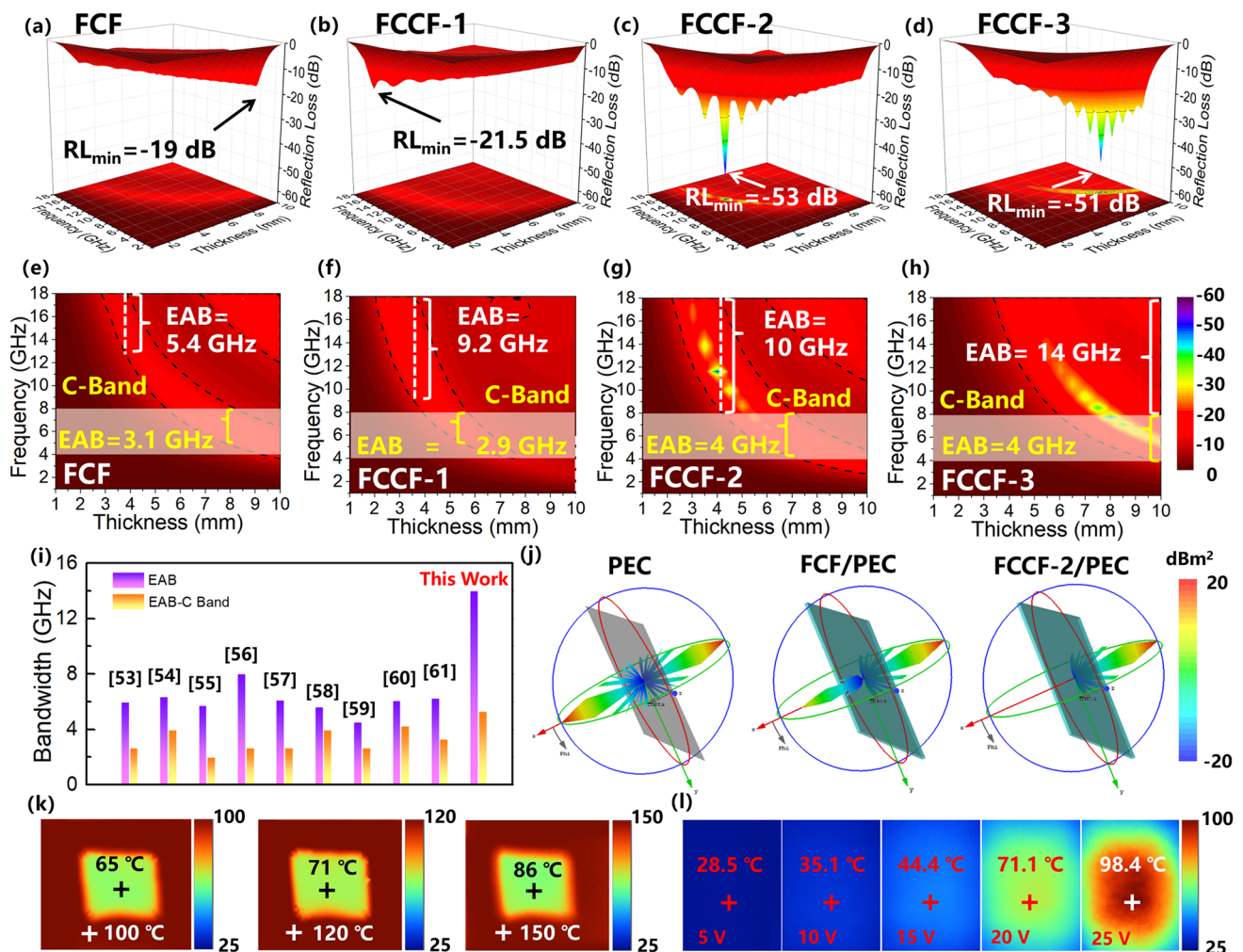


Fig. 4 3D RL values and their projection plots of **a, e** FCF, **b, f** FCCF-1, **c, g** FCCF-2, and **d, h** FCCF-3 samples; **i** comparison of the maximum EAB and the maximum C-Band EAB values with other aerogel/foam-based absorbers reported recently in literature; **j** 3D RCS plots for PEC substrate, PEC substrate covered with FCF and FCCF-2; **k** Infrared radiation images of surface temperature of FCCF-2 sample on a platform with different temperatures; **l** Infrared radiation images of surface temperature of FCCF-2 sample under different driving voltages

performance with surface temperatures ranging from 28.5 to 98.4 °C. It is believed that the 3D interconnected CNC-CF network provides efficient paths for electron transfer, which endows the FCCF-2 sample with excellent electrothermal conversion capability. In a word, the excellent thermal insulation is essential to protect sensitive electronic equipment from high temperatures. Joule heating performance also protects equipment from freezing environments. Therefore, we believe that the composite carbon foam absorbers have the potential to cope with the harsh practical application environment [66–68].

3.3 Microwave Absorption Mechanisms of the Samples

In Fig. 5, the electromagnetic parameters of CF, CCF, FCF, and FCCF-2 samples are further analyzed to investigate the dielectric microwave dissipation mechanisms of the sample. It is shown in Fig. 5a, b that the CF sample exhibits the lowest ϵ' and ϵ'' values, indicating the weak dielectric loss of the CF sample. For the CCF sample, the introduction of the CNCs greatly improves the ϵ' and ϵ'' values, which endows the CCF sample with strong dielectric loss. However, the excessive ϵ' and ϵ'' values result in poor impedance matching (Fig. 3h). Thus, the moderate ϵ' and ϵ'' values endow the FCF and FCCF-2 samples with considerable dielectric loss and good impedance matching. As shown in Fig. S8a, the dielectric loss tangent curves of the samples are calculated. It is observed that the CCF sample exhibits the strongest dielectric loss capability. However, the poor impedance matching of the CCF sample limits the microwave absorption performance. The FCF and FCCF-2 samples both possess strong dielectric loss capability and good impedance matching, resulting in the excellent microwave absorption performance. Therefore, the synergistic effect between the dielectric loss and impedance matching is beneficial for achieving excellent microwave absorption performance. Moreover, the Raman spectra (Figs. 5c and S2c) of the samples all exhibit two characteristic peaks, D-band and G-band peaks, at 1340.1 and 1580.8 cm^{-1} , respectively, indicating the graphitic structures of the samples. In general, the intensity ratio of D-band to G-band (I_D/I_G) stands for the graphitization degree of the graphitic structures [69–72]. It is observed in Figs. 5c and S2c that the CCF and FCCF samples show lower I_D/I_G values compared to the CF and FCF samples,

confirming that the introduction of the CNCs promotes the graphitization degree and enhances the electron transfer capability. For the CCF sample, the growth of the CNCs endows the CCF sample with a dense conductive network, resulting in an excessive electron transport capability. The introduction of magnetic nanoparticles further reduces the electron transport capability of the conductive network. However, in Fig. 5c, the high I_D/I_G value of the CF sample indicates the poor graphitization degree. Thus, the electron transport capability of the CF sample is extremely weak. In this situation, the crystal structures of the magnetic particles improve the electron transport capability of the CF sample instead. Therefore, the introduction of the FeNi/NiFe₂O₄ particles contributes to the moderate ϵ' and ϵ'' values. In addition, the Cole–Cole curves of the samples are calculated to further investigate the polarization loss of the samples according to the Debye relaxation theory [73–76]:

$$\left(\epsilon' - \frac{\epsilon_s + \epsilon_\infty}{2}\right)^2 + (\epsilon'')^2 = \left(\frac{\epsilon_s + \epsilon_\infty}{2}\right)^2 \quad (4)$$

where ϵ_s and ϵ_∞ represent the static permittivity and the relative permittivity at the high-frequency limit, respectively. As presented in Fig. 5d, the CF sample exhibits several semicircles, indicating the existence of multiple polarization processes. Due to the low graphitization degree of CF samples, these polarization processes are attributed to the dipole polarization induced by the defects and functional groups. For the CCF sample, the promoted graphitization degree and the CNC-CF conductive network induce strong conduction loss. Thus, the Cole–Cole curve of the CCF sample shows a linear shape. For FCF and FCCF-2 samples, the electron transfer capability is further adjusted by the FeNi-based nanoparticles. Moreover, the formation of the metal–carbon heterointerfaces induces interfacial polarization. The Raman spectra results show that the FCF and FCCF-2 samples both contain numerous defects, which induce the dipole polarization. Therefore, the Cole–Cole curves of the FCF and FCCF-2 samples show the conduction loss and polarization loss simultaneously. According to the Debye relaxation theory, the transfer of the electrons results in the distortion of the Cole–Cole semicircle. In Fig. 5f, g, the approximately linear curve means that the distortion of the semicircle was at a high level. Thus, conduction loss is the main loss mechanism in dielectric loss. As illustrated

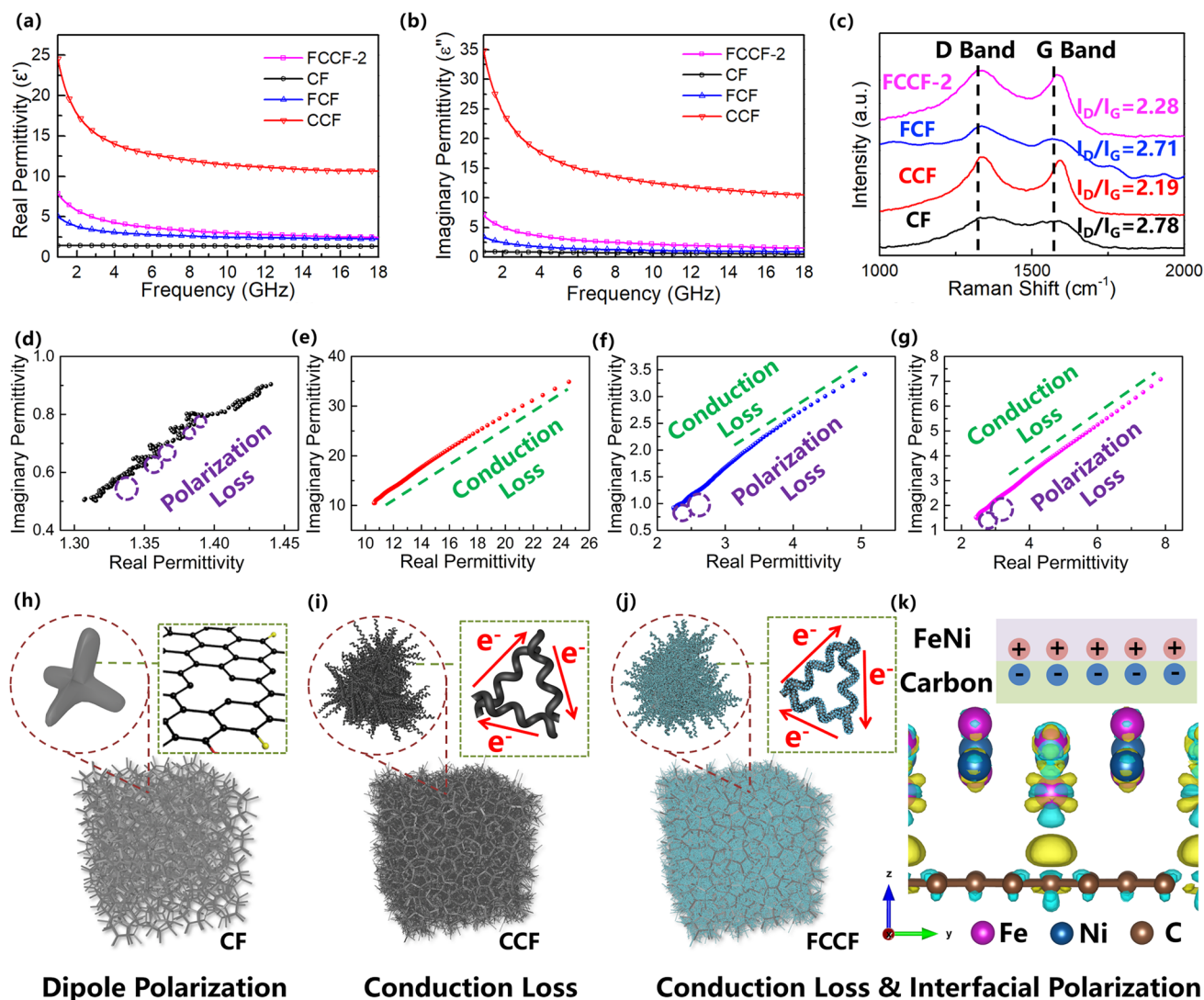


Fig. 5 **a** Real permittivity, **b** imaginary permittivity, and **c** Raman spectra of CF, CCF, FCF, and FCCF-2 samples; Cole–Cole plots of **d** CF, **e** CCF, **f** FCF, and **g** FCCF-2 samples; Dielectric loss diagram of **h** CF, **i** CCF, and **j** FCCF samples; **k** Calculated electron density difference and corresponding isosurface plot. Electron density difference was calculated by $\Delta = \rho(\text{C/FeNi}) - \rho(\text{C}) - \rho(\text{FeNi})$. The yellow and cyan regions denote electron density accumulation and depletion, respectively

in Fig. 5h–k, the dielectric loss mechanisms are presented in accordance with the aforementioned results. Firstly, the main dielectric loss mechanism of the CF sample is dipole polarization due to the poor graphitization degree (Fig. 5h). Secondly, the conduction loss [26] is considered as the main dielectric loss mechanism of the CCF sample due to the formation of the CNC-CF conductive network (Fig. 5i, j). Finally, the introduction of FeNi-based nanoparticles induces interfacial polarization, which is further confirmed by the density functional theory (DFT) calculations (Figs. 5k and S9). Figure 5k provides the calculated electron density

difference and corresponding isosurface plot, in which the yellow and cyan regions denote electron density accumulation and depletion, respectively. It is observed that the charges accumulate at the heterointerface between carbon and FeNi, which induce the interfacial polarization. Moreover, the number of transferred electrons at the carbon-FeNi interface is calculated (Fig. S10), further confirming the existence of the interfacial polarization at the heterointerface between carbon and FeNi. It is reasonable to conclude that the dielectric loss mechanism of FCCF-2 composites could

be attributed to the synergistic effect of the conduction loss and polarization loss.

The permeability of the samples is compared in Fig. 6a, b to further investigate their magnetic loss mechanisms. It is observed that the μ' and μ'' values of the CF and CCF samples are close to 1 and 0, respectively, due to their weak magnetic property. Moreover, the FCF samples exhibit higher μ' and μ'' values due to the formation of the magnetic FeNi-NiFe₂O₄ particles. More importantly, the FCCF-2 sample shows the highest μ' and μ'' values, indicating that the chiral magnetic structure and the nanoscale magnetic heterostructure are beneficial to improve the magnetic loss. In addition, the room-temperature magnetic hysteresis loops (Fig. 6c) are tested to confirm the excellent intrinsic magnetic properties of the FCCF-2 sample. It is observed that the FCCF-2 samples exhibit the highest saturation magnetization (M_s) values, which is consistent with the variation tendency of the μ' and μ'' curves. Figure S2d also shows that the M_s values of the FCCF samples could be well adjusted by modulating the growth density of the magnetic nanoparticles. In the CNC-carbon foam network, the CNCs act as the branches of the carbon foam trunk, increasing the surface area of the sample and providing more growth sites for the magnetic nanoparticles. Therefore, the FCCF-2 sample has a higher saturation magnetization value than the FCF sample. Besides, Figs. 6d and S11 show that the FCF and FCCF samples both show the asymmetry magnetic hysteresis loops, indicating the existence of the exchange bias induced by the FeNi-NiFe₂O₄ magnetic heterostructures. According to the research of Wang et al. [12], the exchange bias originates from the magnetic pinning effect at the interface of the magnetic heterostructures, which is conducive to increasing the magnetocrystalline anisotropy field (H_k). Generally, the H_k could be estimated by comparing the hysteresis loops of the sample using the simplified formulas of the S-W approximation [77, 78]:

$$M = M_s \left(1 - \frac{b}{H^2} \right), H_k = c \cdot b^{\frac{1}{2}} \tag{5}$$

In the above formulae, c is a constant and b is the slope of the $M-1/H^2$ plots. As shown in Fig. 6e, the slope b of the FCCF-2 sample is greater than that of the FCF sample, which indicates that the FCCF-2 sample possesses the larger H_k . According to the Snoke's limit, the larger H_k gives rise to the larger natural resonance frequency, which is beneficial

for improving the magnetic loss. Thus, the eddy current induction coefficient C_0 of the FCF and FCCF-2 samples is calculated ulteriorly to investigate the magnetic resonance [79–82]:

$$C_0 = \mu'' (\mu')^{-2} (f)^{-1} \tag{6}$$

In general, the fluctuations in the C_0 curves indicate the existence of magnetic resonance. According to the ferromagnetic resonance theory, the resonance peaks appearing at 2–10 GHz represent the natural resonance, while the resonance peaks at 10–18 GHz stand for the exchange resonance. As shown in Fig. S8b, the magnetic loss tangent curves of the FCF and FCCF-2 samples are calculated. It is observed that the magnetic loss tangent curves of the FCF and FCCF-2 samples also show several resonance peaks, which is consistent with the C_0 curves. In Figs. 6f and S8b, the FCF and FCCF-2 samples both exhibit natural and exchange resonances. However, the FCCF-2 sample exhibits a higher natural resonance frequency, further confirming that the FCCF-2 sample possesses the larger H_k and promotes the Snoke's limit efficiently.

Furthermore, the dynamic evolution processes of the magnetic domains are explored by the micromagnetic simulations to confirm the magnetic loss mechanisms of the FCF and FCCF-2 samples. Firstly, a magnetic heterostructure composed of the ferrimagnetic NiFe₂O₄ and ferromagnetic FeNi is constructed to confirm the magnetic pinning effect. In Fig. 6g, a magnetic heterostructure composed of the ferrimagnetic NiFe₂O₄ and ferromagnetic FeNi is constructed to confirm the magnetic pinning effect. For the ferromagnetic FeNi, the external alternating magnetic field results in the rotation of magnetic moments. Thus, at the heterointerface between the NiFe₂O₄ and FeNi, the magnetic moment of the ferromagnetic FeNi generates an exchange magnetic field, acting on the uncompensated magnetic moment of the ferrimagnetic NiFe₂O₄. In contrast, the uncompensated magnetic moments around the interface in the ferrimagnetic NiFe₂O₄ also hinder the rotation of magnetic moments in the ferromagnetic FeNi. Therefore, the magnetic loss capability is enhanced by the magnetic pinning effect. Moreover, the microscale linear structure of the FCF sample is constructed by linearly arranging the microscale magnetic particles (Fig. 6h), where the color of the magnetic moments represents the orientations. In Fig. 6h, the multicolor distribution of the

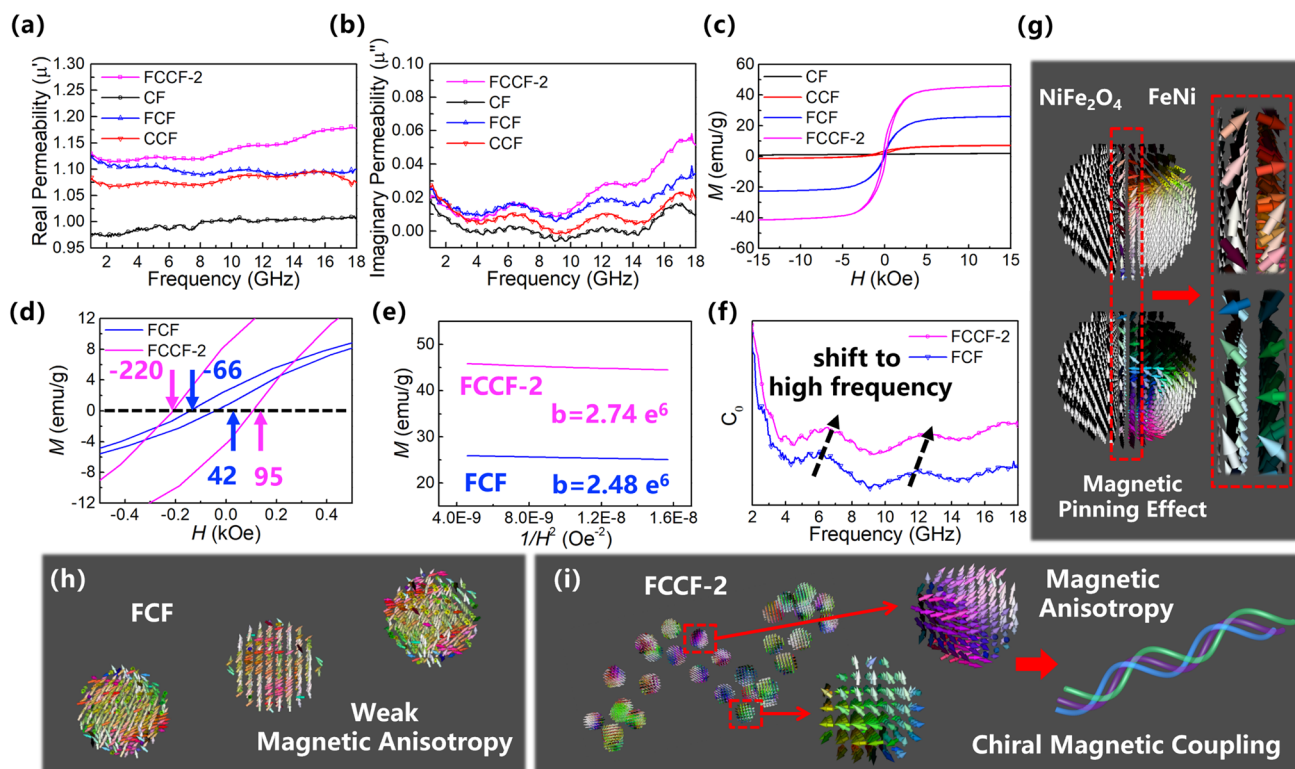


Fig. 6 **a** Real permeability, **b** imaginary permeability, and **c** M-H curves of CF, CCF, FCF, and FCCF-2 samples; **d** Enlarged M-H curves, **e** M versus $1/H^2$ plots, and **f** eddy current induction coefficient of FCF and FCCF-2 samples; micromagnetic simulation of **g** NiFe_2O_4 -FeNi magnetic heterostructures, **h** linear FCF sample, and **i** chiral FCCF-2 sample

FCF sample stands for the chaotic magnetic moment orientations, indicating the weak magnetic anisotropy and weak magnetic coupling. Therefore, the magnetic loss mechanism of the FCF sample is attributed to the rotation of magnetic moments. Moreover, the nanoscale chiral structure of the FCCF-2 sample is also constructed (Fig. 6i). As the magnetic particle size decreases, the magnetic domain orientations tend to be oriented in the same direction, indicating the enhanced magnetic anisotropy. In addition, the magnetic domains in different helical directions show an obvious magnetic coupling effect. In our previous research [29], the enhanced magnetic coupling effect was studied in detail. For the chiral helical structure, the magnetic coupling effects occur not only along the axis of the helical fiber, but also between the helical rings. Thus, it is concluded that the chiral structures enhance the magnetic loss capability of the FCCF-2 sample. In a word, the nanoscale chiral magnetic heterostructures in the FCCF-2 sample achieve strong magnetic anisotropy

and high magnetic loss, which contribute to the excellent microwave absorption performance.

In addition, the quarter-wavelength matching model [30] is introduced to better analyze the microwave absorption mechanisms of the samples:

$$t_m = \frac{n\lambda}{4} = \frac{nc}{4f_m} \frac{1}{\sqrt{|\epsilon_r||\mu_r|}}; n = 1, 3, 5, \dots \quad (7)$$

In the above formulae, the t_m represents the thickness of the absorber, and the f_m stands for the peak frequency of the RL value. Generally, if the t_m and the f_m accord well with the model, the phase cancellation effect would occur to largely reduce the reflection of the microwave. In Fig. S12, the quarter-wavelength matching model curves of the samples are calculated and depicted as the blue dots. It is observed that all the samples accord well with the quarter-wavelength matching model, indicating that the phase cancellation effect contributes to their microwave absorption performance. In addition, Fig. S13 shows that the regions where the

impedance matching values are close to 1 also accord well with the quarter-wavelength matching model. Therefore, it is concluded that the coexistence of the quarter-wavelength matching models and the impedance matching is necessary to obtain the strong microwave absorption performances.

4 Conclusions

In summary, the chiral CNCs are first synthesized on a 3D carbon foam and then combined with the FeNi/NiFe₂O₄ nanoparticles to form a novel chiral-dielectric-magnetic trinity foam via chemical vapor deposition (CVD) and solvothermal reactions. The efficient 3D CNC-CF conductive network provided strong conduction loss, and the formation of metal-carbon interface induced interfacial polarization loss. The nanoscale chiral magnetic heterostructures exhibited magnetic pinning and magnetic coupling effects, further enhancing the magnetic anisotropy and magnetic loss capability. Owing to the synergistic effect between dielectricity, chirality, and magnetism, the trinity composite foam exhibits excellent microwave absorption performance with an ultrabroad EAB of 14 GHz and a minimum reflection of loss less than -50 dB. More importantly, the C-band EAB of the foam is extended to 4 GHz, achieving the full C-band coverage. These results can be used as the guidelines for the design of efficient chiral microwave absorbers.

Acknowledgements This work was supported by the National Natural Science Foundation of China [Grant Nos. 52272288 and 51972039], and the China Postdoctoral Science Foundation [No. 2021M700658]. The authors also acknowledge the assistance of DUT Instrumental Analysis Center.

Authors' Contributions Hao Zhang, Kaili Kuang, Yifeng Zhang, Chen Sun, Tingkang Yuan, Ruilin Yin contributed to conceptualization, data curation, formal analysis, investigation, methodology, visualization, and writing. Renchao Che, Zeng Fan, Lujun Pan contributed to conceptualization, formal analysis, funding acquisition, project administration, resources, supervision, and validation.

Declarations

Conflict of Interest The authors declare no interest conflict. They have no known competing financial interests or personal relationships that could have appeared to influence the work reported in this paper.

Open Access This article is licensed under a Creative Commons Attribution 4.0 International License, which permits use, sharing, adaptation, distribution and reproduction in any medium or format,

as long as you give appropriate credit to the original author(s) and the source, provide a link to the Creative Commons licence, and indicate if changes were made. The images or other third party material in this article are included in the article's Creative Commons licence, unless indicated otherwise in a credit line to the material. If material is not included in the article's Creative Commons licence and your intended use is not permitted by statutory regulation or exceeds the permitted use, you will need to obtain permission directly from the copyright holder. To view a copy of this licence, visit <http://creativecommons.org/licenses/by/4.0/>.

Supplementary Information The online version contains supplementary material available at <https://doi.org/10.1007/s40820-025-01658-8>.

References

1. G. Chen, R. Zhang, M. Yuan, S. Xue, Y. Liu et al., Visualizing nanoscale interlayer magnetic interactions and unconventional low-frequency behaviors in ferromagnetic multishelled structures. *Adv. Mater.* **36**, e2313411 (2024). <https://doi.org/10.1002/adma.202313411>
2. M. He, J. Hu, H. Yan, X. Zhong, Y. Zhang et al., Shape anisotropic chain-like CoNi/polydimethylsiloxane composite films with excellent low-frequency microwave absorption and high thermal conductivity. *Adv. Funct. Mater.* **2316691** (2024). <https://doi.org/10.1002/adfm.202316691>
3. Z. He, H. Xu, L. Shi, X. Ren, J. Kong et al., Hierarchical Co₂P/CoS₂@C@MoS₂ composites with hollow cavity and multiple phases toward wideband electromagnetic wave absorption. *Small* **20**, e2306253 (2024). <https://doi.org/10.1002/sml.202306253>
4. M. Huang, L. Wang, K. Pei, B. Li, W. You et al., Heterogeneous interface engineering of bi-metal MOFs-derived ZnFe₂O₄-ZnO-Fe@C microspheres *via* confined growth strategy toward superior electromagnetic wave absorption. *Adv. Funct. Mater.* **34**, 2308898 (2024). <https://doi.org/10.1002/adfm.202308898>
5. W. Huang, M. Song, S. Wang, B. Wang, J. Ma et al., Dual-step redox engineering of 2D CoNi-alloy embedded B, N-doped carbon layers toward tunable electromagnetic wave absorption and light-weight infrared stealth heat insulation devices. *Adv. Mater.* **36**, 2403322 (2024). <https://doi.org/10.1002/adma.202403322>
6. X. Li, S. Yin, L. Cai, Z. Wang, C. Zeng et al., Sea-urchin-like NiCo₂S₄ modified MXene hybrids with enhanced microwave absorption performance. *Chem. Eng. J.* **454**, 140127 (2023). <https://doi.org/10.1016/j.cej.2022.140127>
7. P. Liu, Y. Li, H. Xu, L. Shi, J. Kong et al., Hierarchical Fe-Co@TiO₂ with incoherent heterointerfaces and gradient magnetic domains for electromagnetic wave absorption. *ACS Nano* **18**, 560-570 (2024). <https://doi.org/10.1021/acsnano.3c08569>
8. X. Liu, Y. Duan, Y. Guo, Z. Li, J. Ma et al., *In situ* construction of complex spinel ferrimagnet in multi-elemental alloy for



- modulating natural resonance and highly efficient electromagnetic absorption. *Chem. Eng. J.* **462**, 142200 (2023). <https://doi.org/10.1016/j.cej.2023.142200>
9. P. Toneguzzo, G. Viau, O. Acher, F. Fiévet-Vincent, F. Fiévet, Monodisperse ferromagnetic particles for microwave applications. *Adv. Mater.* **10**, 1032–1035 (1998). [https://doi.org/10.1002/\(SICI\)1521-4095\(199809\)10:13%3c1032::AID-ADMA1032%3e3.0.CO;2-M](https://doi.org/10.1002/(SICI)1521-4095(199809)10:13%3c1032::AID-ADMA1032%3e3.0.CO;2-M)
 10. L. Yu, G. Lian, G. Zhu, S. Ren, Y. Du et al., Hollow FeCoNiAl microspheres with stabilized magnetic properties for microwave absorption. *Nano Res.* **17**, 2079–2087 (2024). <https://doi.org/10.1007/s12274-024-6468-x>
 11. C. Xu, K. Luo, Y. Du, H. Zhang, X. Lv et al., Anisotropic interfaces support the confined growth of magnetic nanometer-sized heterostructures for electromagnetic wave absorption. *Adv. Funct. Mater.* **33**, 2307529 (2023). <https://doi.org/10.1002/adfm.202307529>
 12. B. Cai, L. Zhou, P.-Y. Zhao, H.-L. Peng, Z.-L. Hou et al., Interface-induced dual-pinning mechanism enhances low-frequency electromagnetic wave loss. *Nat. Commun.* **15**, 3299 (2024). <https://doi.org/10.1038/s41467-024-47537-5>
 13. S. Yang, C. Li, T. Cong, Y. Zhao, S. Xu et al., Sensitivity-tunable strain sensors based on carbon Nanotube@Carbon nanocoil hybrid networks. *ACS Appl. Mater. Interfaces* **11**, 38160–38168 (2019). <https://doi.org/10.1021/acsami.9b12600>
 14. X. Zuo, Y. Zhang, J. Tian, C. Sun, N. Wen et al., Fabrication of micro-mesopores on spiral carbon nanocoils and simultaneous doping with oxygen to expand microwave absorption bandwidth. *Adv. Funct. Mater.* **34**, 2410224 (2024). <https://doi.org/10.1002/adfm.202410224>
 15. C. Sun, H. Zhang, X. Zuo, Y. Jiang, Y. Zhang et al., Integration of carbon microspheres and helical carbon nanocoils for efficient microwave absorption. *Chem. Eng. J.* **498**, 155630 (2024). <https://doi.org/10.1016/j.cej.2024.155630>
 16. H. Chen, C. Wang, Z. Fan, L. Hao, L. Pan, Facile fabrication of binder-free carbon nanotube–carbon nanocoil hybrid films for anodes of lithium-ion batteries. *J. Solid State Electrochem.* **28**, 3325–3335 (2024). <https://doi.org/10.1007/s10008-024-05906-6>
 17. H. Huang, Y. Zhao, T. Cong, C. Li, N. Wen et al., Flexible and alternately layered high-loading film electrode based on 3D carbon nanocoils and PEDOT:PSS for high-energy-density supercapacitor. *Adv. Funct. Mater.* **32**, 2110777 (2022). <https://doi.org/10.1002/adfm.202110777>
 18. S. Xu, Z. Fan, S. Yang, Y. Zhao, L. Pan, Flexible, self-powered and multi-functional strain sensors comprising a hybrid of carbon nanocoils and conducting polymers. *Chem. Eng. J.* **404**, 126064 (2021). <https://doi.org/10.1016/j.cej.2020.126064>
 19. Y. Zhao, H. Zhang, X. Yang, H. Huang, G. Zhao et al., *In situ* construction of hierarchical core–shell Fe₃O₄@C nanoparticles–helical carbon nanocoil hybrid composites for highly efficient electromagnetic wave absorption. *Carbon* **171**, 395–408 (2021). <https://doi.org/10.1016/j.carbon.2020.09.036>
 20. T. Yuan, R. Yin, C. Li, C. Wang, Z. Fan et al., Fully inkjet-printed dual-mode sensor for simultaneous pressure and temperature sensing with high decoupling. *Chem. Eng. J.* **473**, 145475 (2023). <https://doi.org/10.1016/j.cej.2023.145475>
 21. X. Zuo, H. Zhang, C. Zhou, Y. Zhao, H. Huang et al., Hierarchical and porous structures of carbon nanotubes-anchored MOF derivatives bridged by carbon nanocoils as lightweight and broadband microwave absorbers. *Small* **19**, e2301992 (2023). <https://doi.org/10.1002/sml.202301992>
 22. A. Farid, Z. Chen, A.S. Khan, M. Javid, I. Ahmad Khan et al., Ni₃V₂O₈ nanosheets grafted on 3D helical-shaped carbon nanocoils as A binder-free hierarchical composite for efficient non-enzymatic glucose sensing. *Adv. Funct. Mater.* **33**, 2301727 (2023). <https://doi.org/10.1016/adfm.202301727>
 23. Y. Guo, Y. Duan, X. Liu, H. Zhang, T. Yuan et al., Boosting conductive loss and magnetic coupling based on “size modulation engineering” toward lower-frequency microwave absorption. *Small* **20**, 2308809 (2024). <https://doi.org/10.1002/sml.202308809>
 24. A. Farid, A.S. Khan, M. Javid, M. Usman, I.A. Khan et al., Construction of a binder-free non-enzymatic glucose sensor based on Cu@Ni core–shell nanoparticles anchored on 3D chiral carbon nanocoils–nickel foam hierarchical scaffold. *J. Colloid Interface Sci.* **624**, 320–337 (2022). <https://doi.org/10.1016/j.jcis.2022.05.137>
 25. S. Yang, C. Li, X. Chen, Y. Zhao, H. Zhang et al., Facile fabrication of high-performance pen ink-decorated textile strain sensors for human motion detection. *ACS Appl. Mater. Interfaces* **12**, 19874–19881 (2020). <https://doi.org/10.1021/acsami.9b22534>
 26. X. Zuo, Y. Zhao, H. Zhang, H. Huang, C. Zhou et al., Surface modification of helical carbon nanocoil (CNC) with N-doped and co-anchored carbon layer for efficient microwave absorption. *J. Colloid Interface Sci.* **608**, 1894–1906 (2022). <https://doi.org/10.1016/j.jcis.2021.10.065>
 27. Y. Zhao, X. Zuo, Y. Guo, H. Huang, H. Zhang et al., Structural engineering of hierarchical aerogels comprised of multi-dimensional gradient carbon nanoarchitectures for highly efficient microwave absorption. *Nano-Micro Lett.* **13**, 144 (2021). <https://doi.org/10.1007/s40820-021-00667-7>
 28. G. Wang, Z. Gao, S. Tang, C. Chen, F. Duan et al., Microwave absorption properties of carbon nanocoils coated with highly controlled magnetic materials by atomic layer deposition. *ACS Nano* **6**, 11009–11017 (2012). <https://doi.org/10.1021/nn304630h>
 29. H. Zhang, Y. Zhao, M. Yuan, C. Sun, H. Huang et al., Construction of chiral magnetic structure with enhancement in magnetic coupling for efficient low-frequency microwave absorption. *Chem. Eng. J.* **493**, 152692 (2024). <https://doi.org/10.1016/j.cej.2024.152692>
 30. H. Zhang, Y. Zhao, X. Zuo, H. Huang, C. Sun et al., Construction of chiral-magnetic-dielectric trinity composites for efficient microwave absorption with low filling ratio and thin thickness. *Chem. Eng. J.* **467**, 143414 (2023). <https://doi.org/10.1016/j.cej.2023.143414>
 31. P. Song, B. Liu, C. Liang, K. Ruan, H. Qiu et al., Lightweight, flexible cellulose-derived carbon aerogel@reduced graphene oxide/PDMS composites with outstanding EMI

- shielding performances and excellent thermal conductivities. *Nano-Micro Lett.* **13**, 91 (2021). <https://doi.org/10.1007/s40820-021-00624-4>
32. S. Wang, X. Zhang, S. Hao, J. Qiao, Z. Wang et al., Nitrogen-doped magnetic-dielectric-carbon aerogel for high-efficiency electromagnetic wave absorption. *Nano-Micro Lett.* **16**, 16 (2023). <https://doi.org/10.1007/s40820-023-01244-w>
33. S. Shao, S. Xing, K. Bi, T. Zhao, H. Wang et al., Fabrication of graphene/polyimide/Co-N-C aerogel with reinforced electromagnetic losses and broadband absorption for highly efficient microwave absorption and thermal insulation. *Chem. Eng. J.* **494**, 152976 (2024). <https://doi.org/10.1016/j.cej.2024.152976>
34. Y. Zhao, J. Wang, H. Huang, T. Cong, S. Yang et al., Growth of carbon nanocoils by porous α -Fe₂O₃/SnO₂ catalyst and its buckypaper for high efficient adsorption. *Nano-Micro Lett.* **12**, 23 (2020). <https://doi.org/10.1007/s40820-019-0365-y>
35. Y. Zhao, J. Wang, H. Huang, H. Zhang, T. Cong et al., Catalytic anisotropy induced by multi-particles for growth of carbon nanocoils. *Carbon* **166**, 101–112 (2020). <https://doi.org/10.1016/j.carbon.2020.05.007>
36. X. Liang, Z. Man, B. Quan, J. Zheng, W. Gu et al., Environment-stable Co_xNi_y encapsulation in stacked porous carbon nanosheets for enhanced microwave absorption. *Nano-Micro Lett.* **12**, 102 (2020). <https://doi.org/10.1007/s40820-020-00432-2>
37. A. Ahlawat, V.G. Sathe, Raman study of NiFe₂O₄ nanoparticles, bulk and films: effect of laser power. *J. Raman Spectrosc.* **42**, 1087–1094 (2011). <https://doi.org/10.1002/jrs.2791>
38. A. Ahlawat, V.G. Sathe, V.R. Reddy, A. Gupta, Mossbauer, Raman and X-ray diffraction studies of superparamagnetic NiFe₂O₄ nanoparticles prepared by sol–gel auto-combustion method. *J. Magn. Magn. Mater.* **323**, 2049–2054 (2011). <https://doi.org/10.1016/j.jmmm.2011.03.017>
39. F. Pan, M. Ning, Z. Li, D. Batalu, H. Guo et al., Sequential architecture induced strange dielectric-magnetic behaviors in ferromagnetic microwave absorber. *Adv. Funct. Mater.* **33**, 2300374 (2023). <https://doi.org/10.1002/adfm.202300374>
40. F. Pan, K. Pei, G. Chen, H. Guo, H. Jiang et al., Integrated electromagnetic device with on-off heterointerface for intelligent switching between wave-absorption and wave-transmission. *Adv. Funct. Mater.* **33**, 2306599 (2023). <https://doi.org/10.1002/adfm.202306599>
41. N. Qu, H. Sun, Y. Sun, M. He, R. Xing et al., 2D/2D coupled MOF/Fe composite metamaterials enable robust ultra-broadband microwave absorption. *Nat. Commun.* **15**, 5642 (2024). <https://doi.org/10.1038/s41467-024-49762-4>
42. N. Qu, G. Xu, Y. Liu, M. He, R. Xing et al., Multi-scale design of metal–organic framework metamaterials for broadband microwave absorption. *Adv. Funct. Mater.* 2402923 (2024). <https://doi.org/10.1002/adfm.202402923>
43. C.-L. Wang, S. Bai, P.-Y. Zhao, T. Zhou, H.-Y. Wang et al., Metasurface-assisted low-frequency performance enhancement of ultra-broadband honeycomb absorber based on carbon nanotubes. *Nano Res.* **17**, 8542–8551 (2024). <https://doi.org/10.1007/s12274-024-6833-9>
44. R. Xing, G. Xu, N. Qu, R. Zhou, J. Yang et al., 3D printing of liquid-metal-in-ceramic metamaterials for high-efficient microwave absorption. *Adv. Funct. Mater.* **34**, 2307499 (2024). <https://doi.org/10.1002/adfm.202307499>
45. Y. Zhang, S.-H. Yang, Y. Xin, B. Cai, P.-F. Hu et al., Designing symmetric gradient honeycomb structures with carbon-coated iron-based composites for high-efficiency microwave absorption. *Nano-Micro Lett.* **16**, 234 (2024). <https://doi.org/10.1007/s40820-024-01435-z>
46. B. Zhao, Z. Yan, Y. Du, L. Rao, G. Chen et al., High-entropy enhanced microwave attenuation in titanate perovskites. *Adv. Mater.* **35**, e2210243 (2023). <https://doi.org/10.1002/adma.202210243>
47. X. Zhou, H. Zhang, M. Yuan, B. Li, J. Cui et al., Dispersing magnetic nanoparticles into staggered, porous nano-frameworks: weaving and visualizing nanoscale magnetic flux lines for enhanced electromagnetic absorption. *Adv. Funct. Mater.* (2024). <https://doi.org/10.1002/adfm.202314541>
48. J. Xiao, B. Zhan, M. He, X. Qi, X. Gong et al., Interfacial polarization loss improvement induced by the hollow engineering of necklace-like PAN/carbon nanofibers for boosted microwave absorption. *Adv. Funct. Mater.* 2316722 (2024). <https://doi.org/10.1002/adfm.202316722>
49. X. Zhong, M. He, C. Zhang, Y. Guo, J. Hu et al., Heterostructured BN@Co-C@C endowing polyester composites excellent thermal conductivity and microwave absorption at C band. *Adv. Funct. Mater.* **34**, 2313544 (2024). <https://doi.org/10.1002/adfm.202313544>
50. X. Zhang, X. Tian, N. Wu, S. Zhao, Y. Qin et al., Metal-organic frameworks with fine-tuned interlayer spacing for microwave absorption. *Sci. Adv.* **10**, ead1498 (2024). <https://doi.org/10.1126/sciadv.ad16498>
51. X. Zhang, X.-L. Tian, Y. Qin, J. Qiao, F. Pan et al., Conductive metal-organic frameworks with tunable dielectric properties for boosting electromagnetic wave absorption. *ACS Nano* **17**, 12510–12518 (2023). <https://doi.org/10.1021/acsnano.3c02170>
52. X. Meng, J. Qiao, S. Zheng, H. Tian, B. Li et al., Ternary nickel/molybdenum dioxide/carbon composited nanofibers for broadband and strong electromagnetic wave absorption. *Chem. Eng. J.* **457**, 141241 (2023). <https://doi.org/10.1016/j.cej.2022.141241>
53. Y. Zou, X. Huang, B. Fan, J. Yue, Y. Liu, Enhanced low-frequency microwave absorption performance of FeNi alloy coated carbon foam assisted by SiO₂ layer. *Appl. Surf. Sci.* **600**, 154046 (2022). <https://doi.org/10.1016/j.apsusc.2022.154046>
54. C. Cui, L. Geng, S. Jiang, W. Bai, L. Dai et al., Construction of hierarchical carbon fiber aerogel@hollow Co₉S₈ polyhedron for high-performance electromagnetic wave absorption at low-frequency. *Chem. Eng. J.* **466**, 143122 (2023). <https://doi.org/10.1016/j.cej.2023.143122>
55. B.-Y. Lei, Y.-L. Hou, W.-J. Meng, Y.-Q. Wang, X.-X. Yang et al., Hierarchical bath lily-like hollow microspheres constructed by graphene and Fe₃O₄ nanoparticles with enhanced broadband and highly efficient low-frequency microwave

- absorption. *Carbon* **196**, 280–289 (2022). <https://doi.org/10.1016/j.carbon.2022.04.042>
56. J. Liu, L. Zhang, H. Wu, Enhancing the low/middle-frequency electromagnetic wave absorption of metal sulfides through F⁻ regulation engineering. *Adv. Funct. Mater.* **32**, 2110496 (2022). <https://doi.org/10.1002/adfm.202110496>
57. G. Yu, G. Shao, Y. Chen, X. Huang, Nanolayered ceramic-confined graphene aerogel with conformal heterointerfaces for low-frequency microwave absorption. *ACS Appl. Mater. Interfaces* **15**, 39559–39569 (2023). <https://doi.org/10.1021/acscami.3c07988>
58. Q. Chang, H. Liang, B. Shi, H. Wu, Microstructure induced dielectric loss in lightweight Fe₃O₄ foam for electromagnetic wave absorption. *iScience* **25**, 103925 (2022). <https://doi.org/10.1016/j.isci.2022.103925>
59. J. Qiu, X. Liu, C. Peng, S. Wang, R. Wang et al., Porous metal microsphere M@C-rGO (metal = Mn, Fe Co, Ni, Cu) aerogels with high low-frequency microwave absorption, strong thermal insulation and superior anticorrosion performance. *J. Mater. Chem. A* **12**, 21997–22012 (2024). <https://doi.org/10.1039/D4TA04051A>
60. Y. Dong, X. Zhu, F. Pan, L. Cai, H. Jiang et al., Implanting NiCo₂O₄ equalizer with designable nanostructures in agaric aerogel-derived composites for efficient multiband electromagnetic wave absorption. *Carbon* **190**, 68–79 (2022). <https://doi.org/10.1016/j.carbon.2022.01.008>
61. C. Liu, S. Liu, X. Feng, K. Zhu, G. Lin et al., Phthalocyanine-mediated interfacial self-assembly of magnetic graphene nanocomposites toward low-frequency electromagnetic wave absorption. *Chem. Eng. J.* **452**, 139483 (2023). <https://doi.org/10.1016/j.cej.2022.139483>
62. Y. Wu, S. Tan, G. Fang, Y. Zhang, G. Ji, Manipulating CNT films with atomic precision for absorption effectiveness-enhanced electromagnetic interference shielding and adaptive infrared camouflage. *Adv. Funct. Mater.* 2402193 (2024). <https://doi.org/10.1002/adfm.202402193>
63. X. Liu, J. Zhou, Y. Xue, X. Lu, Structural engineering of hierarchical magnetic/carbon nanocomposites *via in situ* growth for high-efficient electromagnetic wave absorption. *Nano-Micro Lett.* **16**, 174 (2024). <https://doi.org/10.1007/s40820-024-01396-3>
64. Y.-L. Wang, P.-Y. Zhao, B.-L. Liang, K. Chen, G.-S. Wang, Carbon nanotubes decorated Co/C from ZIF-67/melamine as high efficient microwave absorbing material. *Carbon* **202**, 66–75 (2023). <https://doi.org/10.1016/j.carbon.2022.10.043>
65. Z. Guo, D. Lan, Z. Jia, Z. Gao, X. Shi et al., Multiple tin compounds modified carbon fibers to construct heterogeneous interfaces for corrosion prevention and electromagnetic wave absorption. *Nano-Micro Lett.* **17**, 23 (2024). <https://doi.org/10.1007/s40820-024-01527-w>
66. S. Zhang, J. Wu, W. Liang, P.-Y. Zhao, H.-Y. Wang et al., Flexible and multifunctional polyimide-based composite films by self-reducing reaction for electromagnetic interference shielding in extreme environments. *Carbon* **212**, 118103 (2023). <https://doi.org/10.1016/j.carbon.2023.118103>
67. Y. Zhang, D. Lan, T. Hou, M. Jia, Z. Jia et al., Multifunctional electromagnetic wave absorbing carbon fiber/Ti₃C₂T_x MXene fabric with ultra-wide absorption band. *Carbon* **230**, 119594 (2024). <https://doi.org/10.1016/j.carbon.2024.119594>
68. T. Zhao, D. Lan, Z. Jia, Z. Gao, G. Wu, Hierarchical porous molybdenum carbide synergic morphological engineering towards broad multi-band tunable microwave absorption. *Nano Res.* **17**, 9845–9856 (2024). <https://doi.org/10.1007/s12274-024-6938-1>
69. U. Ritter, P. Scharff, C. Siegmund, O.P. Dmytrenko, N.P. Kulish et al., Radiation damage to multi-walled carbon nanotubes and their Raman vibrational modes. *Carbon* **44**, 2694–2700 (2006). <https://doi.org/10.1016/j.carbon.2006.04.010>
70. H. Yu, X. Kou, X. Zuo, D. Xi, H. Guan et al., Optimization of multiple attenuation mechanisms by cation substitution in imidazolic MOFs-derived porous composites for superior broadband electromagnetic wave absorption. *J. Mater. Sci. Technol.* **176**, 176–187 (2024). <https://doi.org/10.1016/j.jmst.2023.07.065>
71. Y. Zhao, N. Wang, H. Wang, S. Yuan, M. Liu et al., Chiral structure induces spatial spiral arrangement of Fe₃O₄ nanoparticles to optimize electromagnetic wave dissipation. *Appl. Phys. Lett.* **124**, 161901 (2024). <https://doi.org/10.1063/5.0200510>
72. C. Sun, D. Lan, Z. Jia, Z. Gao, G. Wu, Kirkendall effect-induced ternary heterointerfaces engineering for high polarization loss MOF-LDH-MXene absorbers. *Small* **20**, e2405874 (2024). <https://doi.org/10.1002/smll.202405874>
73. Y. Tian, D. Zhi, T. Li, J. Li, J. Li et al., Graphene-based aerogel microspheres with annual ring-like structures for broadband electromagnetic attenuation. *Chem. Eng. J.* **464**, 142644 (2023). <https://doi.org/10.1016/j.cej.2023.142644>
74. Z. Lin, Y. Hao, H. Huang, Q. He, G. Su et al., Porous carbonaceous aerogels composed of multiscale carbon-based units for high-performance microwave absorption. *ACS Appl. Mater. Interfaces* **15**, 54838–54850 (2023). <https://doi.org/10.1021/acscami.3c13489>
75. Y. Zhao, Z. Lin, L. Huang, Z. Meng, H. Yu et al., Simultaneous optimization of conduction and polarization losses in CNT@NiCo compounds for superior electromagnetic wave absorption. *J. Mater. Sci. Technol.* **166**, 34–46 (2023). <https://doi.org/10.1016/j.jmst.2023.04.045>
76. Z. Jia, L. Sun, Z. Gao, D. Lan, Modulating magnetic interface layer on porous carbon heterostructures for efficient microwave absorption. *Nano Res.* **17**, 10099–10108 (2024). <https://doi.org/10.1007/s12274-024-6939-0>
77. S.J. Collocott, Application of the Stoner-Wohlfarth model with interaction for the determination of the saturation magnetisation, anisotropy field, and mean field interaction in bulk amorphous ferromagnets. *J. Magn. Magn. Mater.* **323**, 2023–2031 (2011). <https://doi.org/10.1016/j.jmmm.2011.03.003>
78. H. Zhang, D. Zeng, Z. Liu, The law of approach to saturation in ferromagnets originating from the magnetocrystalline anisotropy. *J. Magn. Magn. Mater.* **322**, 2375–2380 (2010). <https://doi.org/10.1016/j.jmmm.2010.02.040>

79. Z. Zhou, D. Lan, J. Ren, Y. Cheng, Z. Jia et al., Controllable heterogeneous interfaces and dielectric modulation of biomass-derived nanosheet metal-sulfide complexes for high-performance electromagnetic wave absorption. *J. Mater. Sci. Technol.* **185**, 165–173 (2024). <https://doi.org/10.1016/j.jmst.2023.11.010>
80. M. Han, D. Lan, Z. Zhang, Y. Zhao, J. Zou et al., Micro-sized hexapod-like CuS/Cu₉S₅ hybrid with broadband electromagnetic wave absorption. *J. Mater. Sci. Technol.* **214**, 302–312 (2025). <https://doi.org/10.1016/j.jmst.2024.07.014>
81. P. Wu, X. Kong, Y. Feng, W. Ding, Z. Sheng et al., Phase engineering on amorphous/crystalline γ -Fe₂O₃ nanosheets for boosting dielectric loss and high-performance microwave absorption. *Adv. Funct. Mater.* **34**, 2311983 (2024). <https://doi.org/10.1002/adfm.202311983>
82. J. Du, T. Li, Z. Xu, J. Tang, Q. Qi et al., Structure–activity relationship in microstructure design for electromagnetic wave absorption applications. *Small Struct.* **4**, 2300152 (2023). <https://doi.org/10.1002/sstr.202300152>

Publisher's Note Springer Nature remains neutral with regard to jurisdictional claims in published maps and institutional affiliations.

